TITLE: Systematic Transmission Electron Microscopy-Based Identification of Cellular Degradation Machinery

AUTHORS AND AFFILIATIONS:

Kit Neikirk[1*], Zer Vue[2*], Prasanna Katti[3*], Jianqiang Shao[4], Trace Christensen[5], Edgar Garza Lopez[6], Andrea Marshall[2], Caroline B. Palavicino-Maggio[7], Jessica Ponce[8], Ahmad Alghanem[9], Larry Vang[2], Heather K. Beasley[2,10], Taylor Rodman[2], Margaret Mungai[11], Marcelo Correia[12], Vernat Exil[13], Sandra A. Murray[14], Jeffrey L. Salisbury[5,15], Brian Glancy[3,16], Renata O. Pereira[12,17#], E. Dale Abel[12,17#], Antentor O. Hinton, Jr.[2,6#]

[1] Daniel K. Inouye College of Pharmacy, University of Hawaii at Hilo, Hilo, HI

[2] Department of Molecular Physiology and Biophysics, Vanderbilt University, Nashville, TN

[3] National Heart, Lung, and Blood Institute, National Institutes of Health, Bethesda, MD

[4] Central Microscopy Research Facility, University of Iowa, Iowa City, IA

[5] Microscopy and Cell Analysis Core Facility, Mayo Clinic, Rochester, MN

[6] Hinton and Garza Lopez Family Consulting Company, Iowa City, IA

[7] Department of Neurobiology, Harvard Medical School, Boston, MA

[8] School of Medicine, University of Utah, Salt Lake City, UT

[9] Eastern Region, King Abdullah International Medical Research Center, King Saud bin Abdulaziz University for Health Sciences, Al Hasa, Saudi Arabia

[10] Department of Biochemistry, Cancer Biology, Neuroscience and Pharmacology, School of Graduate Studies and Research, Meharry Medical College, Nashville, TN 37208, USA

[11] Department of Molecular and Cell Biology, University of California Berkeley, Berkeley, CA

[12] Department of Internal Medicine, University of Iowa, Carver College of Medicine, Iowa City, IA

[13] Department of Pediatrics, University of Iowa, Carver College of Medicine, Iowa City, IA

[14] Department of Cell Biology, School of Medicine, University of Pittsburgh, Pittsburgh, PA

[15] Department of Biochemistry and Molecular Biology, Mayo Clinic, Rochester, MN.

[16] National Institute of Arthritis and Musculoskeletal and Skin Diseases, National Institutes of Health, Bethesda, MD

[17] Fraternal Order of Eagles Diabetes Research Center, Iowa City, IA

*These authors share co-first authorship.

#These authors share senior authorship.

Corresponding Author Antentor O. Hinton, Jr.

Department of Molecular Physiology and Biophysics

Vanderbilt University

antentor.o.hinton.jr@Vanderbilt.Edu

319-383-3095

Graphical Abstract:

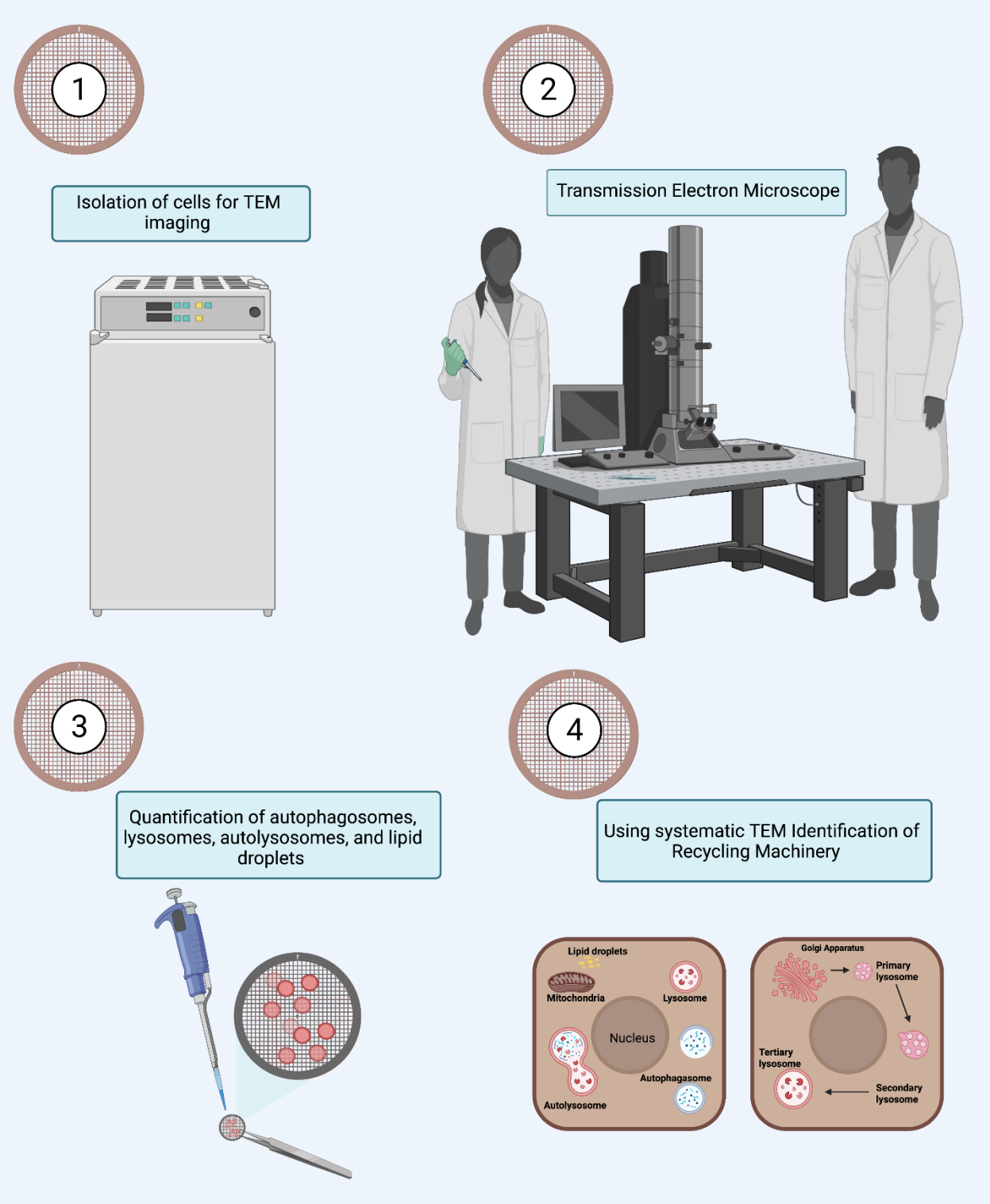

ABSTRACT

Autophagosomes and lysosomes work in tandem to conduct autophagy, an intracellular degradation system which is crucial for cellular homeostasis. Altered autophagy contributes to the pathophysiology of various diseases, including cancers and metabolic diseases. Although many studies have investigated autophagy to elucidate disease pathogenesis, specific identification of the various components of the cellular degradation machinery remains difficult. The goal of this paper is to describe an approach to reproducibly identify and distinguish subcellular structures involved in autophagy. We provide methods that avoid common pitfalls, including a detailed explanation for how to distinguish lysosomes and lipid droplets and discuss the differences between autophagosomes and inclusion bodies. These methods are based on using transmission electron microscopy (TEM), capable of generating nanometer-scale micrographs of cellular degradation components in a fixed sample. In addition to TEM, we discuss other imaging techniques, such as immunofluorescence and immunogold labeling, which can be utilized for the reliable and accurate classification of cellular organelles. Our results show how these methods may be employed to accurately quantify the cellular degradation machinery under various conditions, such as treatment with the endoplasmic reticulum stressor thapsigargin or the ablation of dynamin-related protein 1.

INTRODUCTION

Autophagy is the mechanism by which intracellular components or damaged organelles are removed and degraded to maintain cellular homeostasis [1]. Autophagy is closely linked to apoptosis, and impaired autophagy can be harmful. Although still poorly understood, autophagy

regulation is critical for cellular homeostasis and has been broadly implicated in disease pathogenesis [2]. Autophagic balance is important, as both overactive and underactive autophagy can have negative consequences, such as the malignant transformation and cellular proliferation in cancer or the accumulation of ineffective cells in neurodegenerative diseases [2,3]. The autophagic processes can differ depending on the activation pathway, and autophagy can be either nonselective or selective for specific organelles or proteins in the cell [1,2]. The growing interest in neurodegenerative and other diseases in which autophagy is implicated has highlighted the consequential roles played by autophagy in key biological processes [1,4].

Autophagy is a complex and regulated process involving a variety of structures that contribute to the cellular recycling machinery central of which are autophagosomes and lysosomes. Typically, autophagy is divided into five main stages: initiation, elongation, autophagosome formation, fusion, and degradation [1–3]. During the initiation stage, triggered for example by amino acid starvation, sack-like structures that are precursors of autophagosomes, called phagophores, assemble at sites at the mitochondria-associated endoplasmic reticulum (ER) membrane (MAM) [5]. Proximal to the ER, the phagophore can be observed as an empty, unclosed membrane that elongates and recruits excess materials and cargo for recycling. As materials are delivered to the phagophore, the membrane closes to seal the organelle, transforming the phagophore into an autophagosome, a carrier for cytoplasmic components, cargo proteins or organelles designated for degradation. The autophagosome then fuses with the lysosome, which contains various hydrolases and permeases, and this results in the formation of a autolysosome. Upon fusion, the autophagosome releases its contents into the autolysosome, allowing lysosomal enzymes to initiate the degradation process. Lysosomal hydrolases degrade the materials collected by autophagosomes, and the resulting macromolecules are released through permeases.

Autolysosomes are impermeant structures that are dissolved upon the completion of this process. The components of the autolysosomes can be used to reform lysosomes or become components of new phagophore membranes, whereas the macromolecules released into the cytosol can then be recycled for use in other biological functions [1–3,6].

Transmission electron microscopy (TEM) has advanced the field of autophagy research by enabling the study of subcellular characteristics at high resolution [4]. Specifically, TEM works by transmitting electrons through ultrathin sections of fixed and embedded samples, generating nanometer scale micrographs that allow for careful study of all the processes formed throughout autophagy [7–9]. For example, TEM has facilitated the identification of unique autophagic structures, revealing that autophagosomes are formed at ER contact sites and has delineated the five-stage maturation process described above [7,9]. Our method utilizes ImageJ software for the analysis of TEM micrographs of autophagic components [10]. ImageJ is a free, open-source platform that enables the quantification and statistical analysis of images [8]. This study proposes the application of a method that was adapted and optimized based on an established method for using TEM to analyze mitochondria and ER, recently described by Lam et al. [8].

The success of the protocol presented here is depends on proper identification of the cellular degradation components. Lysosomes can present with diverse morphologies, which can complicate their specific identification. The morphology of lysosomes is usually depicted as a spherical shape, ranging from 0.05 to 0.2 micrometers in diameter (Figure 1A–C; Table 1) [11]. Lysosomes typically aggregate in the center of many types of cells; however, differing intracellular conditions, such as raised pH, have been demonstrated to cause lysosomes to migrate toward the cell membrane [12]. Lysosomes can be classified as primary, secondary, or tertiary, depending on their digestive activities and the process through which they are formed. Further complicating

lysosome identification is the frequent tendency of lysosomes to feature multiple membranes [13], resulting in an appearance similar to that observed for multilamellar bodies (MLBs; Figure 1L–M; Table 1), which are liposomes that contain lipids within a central compartment surrounded by many membrane bilayers [14]. Lysosomal membranes feature inner folds that are highly organized, and the enzymes contained within lysosomes have a distinct, darker, and more consistent appearance versus the lipids typically found in MLBs (Figure 1A–C, L-M; Table 1). The lipids found in MLBs can also appear as dots that speckle the MLB interior, which can be used to differentiate MLBs from lysosomes, although these dots can also be mistaken for cargo in secondary lysosomes (Figure 1A-C; Table 1). Even with these considerations, the accurate and reproducible identification of lysosomes based solely on TEM imaging may be inconsistent, necessitating the application of additional imaging techniques, such as fluorescent staining. Not only is there a need to positively identify lysosomes, but it is critical that autophagosomes be identified, characterized, and distinguished from lysosomes as well as other structures.

The appearance of autophagosome can also vary depending on their cargoes, which can make their identification challenging (Figure 1K–L; Table 1). Ideally, an autophagosome can be identified by the presence of a clear double-limiting membrane, separated by a short distance, that appears darker than the rest of the TEM image (Figure 1K; Table 1). However, autophagosomes may also appear with only a single membrane or with several separate membranes (Figure 1K–L; Table 1) [15]. These diverse membrane presentations can lead to the misidentification of malformed mitochondria or ring-shaped ER that present with appearances similar to those of autophagosomes (Figure 1D–E; Table 1). During identification, the inclusion or exclusion of certain types of autophagosomes can be performed. If the structures appear empty or lacking in material, these structures are likely not involved in degradation, and they may be excluded;

however, care must be taken not to mistake empty autophagosomes for lipid droplets (LDs; Figure 1F–J; Table 1). Similarly, if the body is a phagophore that has not yet closed to form an autophagosome, this structure is not yet used for recycling and can be inadvertently identified as an autophagosome [4,15]. Some autophagosomes can be observed in the process of fusing with a lysosome but cannot yet be considered an autolysosome, and some studies have classified these structures as autophagolysosomes or autophagosome–lysosome fusions. These structures can be included in autolysosome or autophagosome quantifications if their inclusion is consistent [1,2]. These intermediate structures can be identified by their much larger appearance, and the contents inside the lysosome and the autophagosome often appear to be interacting.

When autophagosomes contain smaller volumes of cargo materials (Figure 1D-E; Table 1), they can mimic large, irregularly shaped lysosomes with a double-limiting membrane (Figure 1B; Table 1) [1,11]. Furthermore, lipids are not reliably preserved during sample preparation, resulting in variations in the appearance of limiting membranes depending on the methods used [15]. Autophagosomes can also resemble multi-inclusion bodies and multivesicular bodies (MVBs), which are also known as pre-vacuolar compartments that serve as an intermediary structure between vacuoles and the *trans*-Golgi network (Figure 1L-N; Table 1) [16]. Although these structures are related to autophagy, they are different from autophagosomes and should not be included in quantifications of autophagosomes [17]. Typically MVBs and MLBs only display a single membrane (Figure 1L; Table 1); therefore, the presence of a second membrane, in addition to the identification of inner recycled ribosomes, more circular shapes representing cargo, or more internal lipids, are all characteristic of autophagosomes (Figure 1D; Table 1) [14,15]. Additionally, MVBs are generally smaller than autophagosomes and lysosomes, whereas MLBs are larger, sometimes reaching a size ten times that of a typical lysosome [11,14]. Furthermore,

autolysosomes (Figure 1C-E; Table 1) may also be mistaken for LDs (Figure 1F–J; Table 1) or lysosomes (Figure 1A–C; Table 1). Careful consideration of these features should occur to ensure proper identification of these respective organelles.

Ultrastructural characteristics of other organelles can be used to distinguish them from autophagic components. For example, the presence of ribosomes, which typically appear as small black dots around the edge of an unidentified structure, or the observation of a thinner width that wraps around other organelles, such as mitochondria, are strong ER structural indicators. Similarly, evidence of mitochondrial cristae or the folds of the mitochondrial inner membrane can be used to identify mitochondrial structures. However, the exact identification of specific organelles can be challenging, despite awareness of the typical characteristics of other organelles. For example, partially degraded ribosomes can aggregate in autophagosomes, thus appearing as either speckled ribosomes or dark clumps, which increases the likelihood of mistaking an autophagosome for rough ER [15].

Although the basic processes involved in autophagosome formation are understood, many of the nuances of the degradation machinery and the specific pathways involved, require further elucidation. Many downstream effects of autophagy are important. For example, LDs store lipids that can be mobilized to provide a source of energy retrieval when necessary. Like all organelles, LDs can be targeted by autophagy for recycling; however, interestingly, the macromolecules released at the end of autophagy can be stored in newly formed LDs, even under starvation conditions, to avoid lipotoxicity [18]. Therefore, one downstream consequence of autophagy, which could evidence ongoing autophagy, is an increase in the presence of LDs within a cell. LDs protect against ER stress and may serve as a protective barrier against mitochondrial autophagy, known as mitophagy, by forming close mitochondria-to-lipid contacts [19]. Autophagy impacts

nearly every cellular organelle due to its role in organelle degradation; for example, ER stress can trigger the onset of autophagy to recycle the damaged ER membranes and contribute to the generation of a healthy ER [20]. Similarly, impaired mitochondrial fission or other forms of mitochondrial dysfunction due for example to impaired function of critical regulatory proteins, such as mitofusin 1 (MFN1), can trigger mitophagy to clear ineffective mitochondria [21,22]. Because all organelles interact with the cellular degradation machinery, understanding the dynamics between the primary recycling organelles—lysosomes, autophagosomes, and autolysosomes—and other organelles will be important to fully appreciate the contributions and drivers of the autophagic process. Careful and accurate identification of components of the autophagic machinery will be important for advancing knowledge of the effectiveness of therapeutics, whose mechanisms of action may involve autophagy. Furthermore, this may result in further elucidation of pathways that induce autophagy and may clarify how autophagy contributes to disease prevention and progression [23]. Accurate characterization and quantification of autophagic machinery components require the proper identification of these degradation organelles and other subcellular structures involved in the autophagic process.

Although many studies have identified components of the autophagosome and lysosome machinery, further elaboration of detailed methods for identifying and quantifying these organelles using rigorous techniques remains critical for establishing standardized protocols for comparison of data between groups [7,15,24–26]. Previous studies have not consistently evaluated other important degradation machinery components, such as LDs and autolysosomes, and have not considered some of the nuances associated with these organelles. Many of these structures are similar, but they can differ from cell to cell and are easily misidentified. A basic understanding of the various potential and common appearances of lysosomes and autophagosomes is critical for

the performance of TEM analysis. Here, we describe the characteristics that should be assessed to properly identify autophagic organelles and provide recommendations for effective classification (Supplementary Figure 1).

Our ultimate aim was to identify and quantify difficult-to-measure autophagic machinery in clear terms and present a novel approach for the measurement all cellular degradation machinery using a free, open-source software program. These techniques can be applied to reproducibly quantify and characterize changes that occur in the organelles associated with autophagy.

MATERIALS & METHODS

Mouse Care & Maintenance

Care of mice was performed based on prior protocols [27] and in accordance with protocols approved by the University of Iowa Animal Care and Use Committee (IACUC). We utilized male C57Bl/6J mice. Animals were housed at 22 °C with a 12-h light, 12-h dark cycle, and free access to water and standard chow. Mice with tamoxifen-inducible knockout of DRP1 in skeletal muscle were generated by crossing mice that harbored a homozygous floxed allele of DRP1 with mice harboring a tamoxifen-inducible Cre recombinase under the control of the myogenin promoter (Jackson Lab) in skeletal muscle as previously described [28,29]. Myotubes were isolated from these mice, using protocols described below.

Fly Strains and Genetics:

A mitochondrial assembly regulatory factor (Marf) knockdown fly was generated according to previous protocols [30]. Genetic crosses were performed on yeast corn medium at 22 °C. W1118

flies were used as genetic background controls. Mef2- Gal4 (III) was used to drive muscle-specific Marf RNAi (BS# 55189) to achieve gene knockdown. Mef2-Gal4 (BS# 27390) stocks were requested or obtained from the Vienna Drosophila Stock Center (VDRC) and Bloomington Drosophila Stock Center. All chromosomes and gene symbols are as mentioned in Flybase (http://flybase.org).

Isolation of Satellite Cells & Differentiation

When adopting this protocol, one individual who is blinded to the mouse genotype or treatment should conduct the experiment, including the isolation, differentiation, and fixation of the murine and human cells. This individual should not be involved in performing later analyses to mitigate introducing bias. Satellite cell isolation and differentiation for thapsigargin treatment and DRP-1 ablation were performed as described previously, with minor modifications [8,27,31]. Once C57B1/J1 mice reached 8–10 weeks of age, mice were placed under anesthesia using isoflurane, and the skeletal muscles of the gastrocnemius and quadriceps were excised and washed twice with 1× phosphate-buffered saline (PBS) supplemented with 1% penicillin-streptomycin and fungizone (300 µL/100 mL). Dulbecco's modified Eagle's medium (DMEM)-F12 media with collagenase II (2 mg/mL), 1% penicillin-streptomycin, and fungizone (300 µL/100 mL) was added to the muscles and shaken for 90 min at 37 °C. This media was removed, the cells were washed with PBS x4 times, and media replaced with DMEM-F12 media with collagenase II (0.5 mg/mL), 1% penicillin-streptomycin, and fungizone (300 µL/100 mL), before being shaken for 30 min at 37 °C. The tissue was then ground until all cells were dislodged from the tissue matrix and were passed through a fine, 70-µm cell strainer. The isolated cells were centrifuged, resuspended, and plated on BD Matrigel-coated dishes. The cells obtained were differentiated into myotubes through

the addition of DMEM-F12, 20% fetal bovine serum (FBS), 40 ng/mL basic fibroblast growth factor (R&D Systems, 233-FB/CF), 1× non-essential amino acids, 0.14 mM β-mercaptoethanol, 1× penicillin/streptomycin, and fungizone (300 µL/100mL). Myotubes were maintained in medium containing 10 ng/mL growth factor until 85% confluency was reached, at which point they were differentiated in DMEM-F12, 2% FBS, 1× insulin–transferrin–selenium.

Preparation of cells for TEM

Cells were fixed with 2.5% glutaraldehyde in sodium cacodylate buffer for 1 h in a cell incubator. They were then embedded in 2% agarose, postfixed in buffered 1% osmium tetroxide, stained in 2% uranyl acetate, dehydrated with an ethanol gradient series, and embedded in EMbed-812 resin. Thin sections were cut on an ultramicrotome and stained with 2% uranyl acetate and lead citrate. Images were acquired by TEM on either a JEOL JEM-1230, operating at 120 kV, or a JEOL 1400, operating at 80kV.

Immunogold Labeling

Immunogold labeling was performed in accordance with prior established protocols [32]. Primary skeletal myotubes were fixed for 2 h in 2% paraformaldehyde (PFA) and 0.125% glutaraldehyde in 0.1 M phosphate buffer. Ultrathin cryosections were prepared, and single- or double-immunogold labeling was performed using antibodies and protein A coupled to gold. Once labeling was completed, they were imaged via TEM.

Lysotracker

The protocol was performed based on prior procedures [33]. LysoTracker™ Red DND-99 (ThermoFisher Scientific, L7528) was diluted to a final concentration of 1 mM with dimethyl sulfoxide (DMSO) to create a stock solution. The stock solution was then mixed with warm growth media to a 1:2000 dilution. Growth media from the cells was aspirated and replaced with the working solution of LysoTracker™ Red DND-99. Cells were imaged live using an SP-8 confocal inverted microscope with a white laser light set to an excitation wavelength of 577 nm and an emission wavelength of 590 nm ± 10 nm. This allowed for a yellowish pseudo coloration to be observed. For the staining of fixed cells, cells were grown in culture media on a #1.5 cover glass, either embedded into a petri dish or divided by plastic-walled growth chambers to optimize microscopic optics. Cells were incubated for 30 min with a working solution of LysoTracker™ Red DND-99. The staining solution was then aspirated from the plate, rinsed, and subsequently fixed in 4% PFA. Confocal image stacks were captured with a Zeiss LSM-5, Pascal 5 Axiovert 200 microscope, using LSM 5 version 3.2 image capture and analysis software and a Plan-APOCHROMAT 40x/1.4 Oil DIC objective. Images were deconvoluted with the National Institutes of Health (NIH) ImageJ software and BITPLANE-Imaris software. Imaris software analysis was used to measure lysosome number, volume, and area. Experiments were conducted in triplicate, at minimum, and 10–20 cells per condition were quantified.

Immunofluorescence

Immunofluorescence was performed according to standard procedures [27,34]. For, live-cell imaging, live cells were plated and imaged in MatTek 35 mm glass-bottom culture dishes and grown on Matrigel. After the cells were grown, they were fixed with 4% (w/v) PFA in PBS for 30 min, followed by permeabilization with 0.25% Triton X-100 in PBS for 10 min at room

temperature. Then, the cells were blocked with 10% bovine serum albumin in PBS. The fixed cells were incubated with rabbit anti-lysosomal associated membrane protein (LAMP-1; Cell Signal: D2D11) antibody in 1% BSA in PBST (PBS + 0.1% Tween 20) at a 1:25 dilution at 4 °C overnight. After 3 PBS washes, each 5 minutes long, Alexa Fluor 488-conjugated goat-rabbit mouse IgG (Life Technologies: A-11008) secondary antibodies were added at 1:1000 dilution in 1% BSA and incubated at room temperature for 45 minutes in the dark. After another 3 PBS washes, the coverslips were mounted onto glass slides with ProLong Diamond Antifade with 4',6-diamidino-2-phenylindole (DAPI) and allowed to dry overnight. Confocal image stacks were captured with a Zeiss LSM-5, Pascal 5 Axiovert 200 microscope, using LSM 5 version 3.2 image capture and analysis software and a Plan-APOCHROMAT 40x/1.4 Oil DIC objective. Imaris software analysis was used to measure lysosome intensity, length, and sphericity. Experiments were performed in triplicate, at minimum, and 10–20 cells per condition were quantified.

Human Myotubes

GIBCO® Human Skeletal Myoblasts were obtained (ThermoFisher Scientific, A1255). Cells were thawed and plated in HG DMEM containing 1% penicillin/streptomycin, 1% fungizone, and 2% horse serum. Cells were differentiated after 48 h, and myotubes were extracted. Fibroblasts were grown *in vitro* to the third passage and plated in 6-well tissue culture plates (5×10^5 cells per well) in DMEM (Invitrogen) supplemented with 10% heat-inactivated fetal bovine serum, 100 U/ml of penicillin, 100 µg/ml of streptomycin, 0.25 µg/ml of fungizone, 1 mm sodium pyruvate, and 10 mm HEPES at 37 °C in a humidified incubator with 10% CO_2. Cells were infected with Ad-Cre, while Ad-GFP was a control.

Thapsigargin Treatment

Myotubes and fibroblasts were treated with thapsigargin in accordance with prior methods [8,35]. Fibroblasts, human myotubes, and mouse myotubes were treated with thapsigargin (2 μg mL^{-1}; Sigma) for 10 h, followed by crosslinking with 1% formaldehyde, which was performed for 10 min.

Systematic ImageJ Parameters and Measurement

We utilized documented parameters and quantification methods [8]. A unique individual was responsible for imaging the entire cell at low magnification. Obtained images were uploaded to ImageJ using an acceptable format, such as TIFF. The cell was then be divided into quadrants using the ImageJ plugin quadrant picking (https://imagej.nih.gov/ij/plugins/quadrant-picking/index.html, accessed August 21, 2021). This ensured random and unbiased selection of quadrants for quantification. Once the image was sectioned into four quadrants, two of these quadrants were randomly selected for complete analysis. Three independent, blinded individuals were tasked with performing the quantification of these quadrants according to the protocol described below. Their collective findings were averaged to decrease individual subjective bias. To ensure accurate and reproducible values, measurements were repeated for a minimum of 10 cells each. In future experiments, if significant variability is observed across the three individuals performing the analysis, increasing the sample number (n) by expanding the number of cells quantified was found to decrease variability.

All analysis methods were developed using NIH ImageJ software. Necessary measures should be set on ImageJ prior to analysis (Analyze > Set Measurements: Area, Mean gray value, Min & Max gray value, Shape descriptors, integrated density, Perimeter, Fit ellipse, Feret's Diameter).

Measurements of lysosomes, autolysosomes, LDs, and autophagosomes, including area, circularity, and length, were made using the Multi Measure region of interest (ROI) tool in ImageJ and were based on established measurements [8,36]. The freehand tool in NIH ImageJ 1.49 was used to manually trace the cellular degradation machinery membrane to determine the area or volume. A 19 × 23 cm rectangular grid was overlaid on each image to quantify cellular degradation structures in each image, and the numbers were presented per 10 μm^2 of the cytoplasm.

Statistical Analysis

The results are presented as the mean ± standard error of the mean (SEM). Data were analyzed using unpaired Student's T-tests. If more than two groups were compared, one-way analysis of variance (ANOVA) was performed, and significance was assessed using Fisher's protected least significance difference test. For T-tests and ANOVA, the GraphPad and Statplus software package was used (SAS Institute, Cary, NC). For all statistical analyses, significant differences were accepted when $p < 0.05$.

PROTOCOL:

1. *Downloading and Preparing ImageJ Software for Analysis*
    1.1. Download ImageJ software from the official NIH website (https://imagej.nih.gov/ij/download.html).
    1.2. Install and open the ImageJ software.
    1.3. Select **Analyze ▸ Tools ▸ ROI Manager** to open the ROI Manager, which is used to record and track measurements.

1.4. Click on **Analyze ▸ Set Measurements** to input the measurements for ImageJ to perform, such as area, circularity, and perimeter.

1.4.1. For the current protocol, area and count will be the focus; however, all available measurements may be utilized, depending on the aims of the study.

1.5. Import the image to be analyzed (a TIFF or DM3 file is recommended due to their high quality) directly into ImageJ.

1.5.1. Alternatively, click **File ▸ Open** to open the selected image.

1.6. Considerations

1.6.1. For accuracy and reproducibility, ensure that each image contains a scale bar, bar length, and image magnification. The scale bar and bar length are important for setting the appropriate units within the ImageJ settings.

1.6.2. Quantification of samples should be performed by three individuals in a randomized and blinded manner to ensure an unbiased approach.

1.6.3. To save time, images may be divided into quadrants, and the same quadrants should be analyzed across all images.

2. *Analyzing Lysosomes, Autophagosomes, and Autolysosomes (Supplementary Figure 2A–C)*

2.1. Click on **Freehand Selections** to access the **Freehand** tool.

2.2. Trace the outline of the entire cell.

2.3. Click **Add** on the ROI Manager. This ROI will be used to normalize later measurements.

2.4. To obtain the length and width, use the **Straight-Line** tool to draw a line down the major and minor axes of each organelle (Supplementary Figure 2A–C, Step 1).

2.5. Trace the membrane of each lysosome, autophagosome, or autolysosome. Add the shape to the ROI Manager (Supplementary Figure 2A–C, Step 2).

2.6. Click **Measure** in the ROI Manager to obtain measurements for the area.

2.7. Add the measurements to the ROI Manager and use the **Measure** function to obtain numerical values for each measurement.

2.8. Considerations

2.8.1. Ensure that autophagosomes, lysosomes, and autolysosomes are being measured separately because the ROI Manager will group all functions together for statistical analysis.

2.8.2. The number of autophagosomes, lysosomes, or autolysosomes counted in the cell should be normalized against the total cell area.

3. Analyzing Lipid Droplets

3.1. Repeat Steps 2.1–2.5 for LDs to obtain the basic measurements needed for analysis (Supplementary Figure 2D).

3.2. For each cell, calculate the total area of all LDs. The amount of lipid coverage is the total area of all LDs divided by the total cell area.

3.2.1. This process can be used to determine the percent coverage of other subcellular structures, including mitochondria and recycling machinery.

3.3. Contact sites between organelles can be measured by first using the **Freehand** tool to trace the outer membranes of both subcellular structures being analyzed, as described in Step 2.4 (Supplementary Figure 2D, Step 1).

3.4. To determine the contact site length, click on the **Straight, Segmented, or Freehand Lines** tool on the toolbar, and select **Freehand Line**. Draw a line spanning the length of the contact site, add the measurement to the ROI Manager, and use the **Measure** function to determine the length of the contact (Supplementary Figure 2D, Step 2).

3.5. The contact distance may be similarly measured by using the **Freehand Line** tool to draw a line between the two objects being measured.

3.6. To calculate percent coverage, simply divide the cumulative contact lengths by the percent coverage of one of the two subcellular features in question, as determined in Step 3.2, and multiply the value by 100 to obtain a percentage.

REPRESENTATIVE RESULTS:

This protocol describes a method for obtaining reproducible measurements and the identification of structures involved in the autophagic process. Below, we discuss the results obtained using this TEM image analysis approach.

Identification of organelle compartments by immunogold labeling

Considering some of the pitfalls associated with correctly identifying organelles by TEM morphology alone, other methods may be required to monitor organelles. One of the most effective alternatives is the immunogold labeling technique used in electron microscopy to analyze organelle marker proteins. In mitochondria, the mitochondrial GTPase proteins mitofusin 1 and 2 (MFN1 and MFN2) function in mitochondrial fusion reactions [21,22,37–40]. Thus, mitochondria

can be readily identified by MFN1 in tissues due to the formation of MFN1-positive puncta (Figure 1O–P).

The fundamental concept of immunogold labeling can be applied to organelles associated with autophagy. Many novel yeast genes that are essential for autophagy (autophagy-related, or ATG genes) have been characterized, and most of their mammalian homologs have been identified [41]. Microtubule-associated protein 1 light chain 3 (LC3) is the mammalian homolog of Atg8 [42] and is a reliable marker for autophagosomes in mammals. Thus, autophagosomes can be positively identified by the formation of LC3-positive puncta (Figure 1Q–R). The expression levels of LC3 in different autophagosomes (Figure 1, blue arrows) and phagosomes (not shown) may be variable due to the degradation of LC3 by lysosomal hydrolases, which can make the identification of late-stage autophagic materials more challenging [43]. However, the identification of LC3-positive puncta remains beneficial for the identification of autophagosomes. Immunogold labeling has also been performed with caveolin-1 (CAV-1), which is a marker protein for specialized membrane domains known as caveolae, which ultimately accumulate in caveosomes that mature into MVBs upon endocytosis [44]. Therefore, CAV-1 immunogold labeling can be used to identify MVBs (Figure 1S–T), and the presence of CAV-1 puncta in an ROI can be used to exclude those vesicles from classification as autophagosomes, indicating instead the presence of a multivesicular or multi-inclusion body. After we tested immunogold labeling, we examined changes in the cellular degradation machinery under other conditions.

Thapsigargin treatment alters lysosome, autolysosome, and autophagosome morphology

We also investigated the morphological changes that occurred in lysosomes, autolysosomes, and autophagosomes in response to thapsigargin treatment (Figure 2). Thapsigargin is a sarcoplasmic-ER Ca^{2+}-ATPase (SERCA) inhibitor, and thapsigargin treatment

in cells causes a decrease in the lengths of mitochondria–ER contacts while also inducing ER stress [8,45]. Using our TEM image analysis protocol, we found that both the mean lysosomal area and the number of lysosomes per square micron significantly increased in response to thapsigargin treatment in primary mouse skeletal myotubes (Figure 2E–F). The mean area of autolysosomes and the number of autolysosomes per square micron showed an even greater increase than the values for lysosomes (Figure 2G–H). The mean autophagosomal area and the number of autophagosomes per square micron also significantly increased in thapsigargin-treated cells (Figure 2I–J). Similar results were demonstrated in both mouse fibroblasts (Figure 2K–T) and human myotubes (Figure 2U–AD). Human myotubes displayed the largest increases in autophagy recycling machinery for all assessed components. Accompanying these quantifications are representative images for each cell type (Figure 2A–D, K–N, and U–X). Thapsigargin inhibits ER function and promotes cellular stress, and these findings support a model in which cell-stress-induced organellar damage increases the activity of machinery, including lysosomes and autophagosomes, to degrade damaged organelles. Thus, the morphological changes detected and quantified using the TEM method are consistent with the expected effects of thapsigargin treatment.

DRP-1 ablation results in increased degradation machinery

Dynamin-related protein (DRP-1) is a crucial protein involved in the regulation of mitochondrial fission [29,46]. Other studies have reported that the impaired mitochondrial fission can have downstream effects on organellar morphology and function throughout the cell [47]. In the absence of DRP-1, mitochondria undergo fission less frequently, resulting in longer mitochondria that can trigger potential downstream effects, including apoptosis [46]. To test our method, we generated a skeletal muscle-specific DRP-1 knockout mouse and observed changes in

the degradation machinery. Specifically, our study focused on lysosomes, autophagosomes, and LDs, which are all closely linked to the process of autophagy. For lysosomes, we investigated the effects of DRP-1 ablation in a skeletal myotube-specific knockout model (DRP-1smKO), which resulted in a significant and large increase in lysosome numbers compared with the wild-type control (Figure 3A–F, red arrows). Additionally, we observed increases in both the number of lysosomes per square micron and the lysosomal area per square micron, although the change in lysosomal area was not as great as the absolute change in lysosome number (Figure 3G–H). Similarly, DRP-1smKO also resulted in a significant and large increase in the autophagosome number compared with the wild-type control (Figure 3I–L, red arrows). Additionally, we observed increases in both the number of autophagosomes per square micron and the autophagosomal area per square micron, although the change in area was less than the absolute change in number (Figure 3M–N). For both results, based on the change in percentage and the degree of significance, the increase in autophagosomes was greater than the increase in lysosomes, which suggested that reduced mitochondrial fission may cause larger shifts in the formation of cargo vessels than in the formation of lysosomes, although both types of organelles increased significantly. Autophagosome–lysosome fusion events may also contribute to this disparity, as during the intermediate fusion phase, these structures more closely resemble autophagosomes than lysosomes.

To further validate these results, we also used fluorescent dyes to image lysosomes in DRP-1smKO myotubes. LysoTracker is a fluorescent dye used to label and track acidic organelles in live cells, which can be used to effectively identify the highly acidic lysosomes. Similar to the TEM data, the LysoTracker assay showed that DRP-1smKO resulted in a significant increase in lysosomes compared with the wild-type control (Figure 3O-P). Increases in lysosomal number,

lysosomal calculated volume, and lysosomal area were also observed in DRP-1 knockout mice (Figure 3Q–S). These key quantifications are similar to the quantifications determined by TEM analysis; however, LysoTracker analysis provides better certainty that lysosomes are being measured. Lysosomes can also be identified by LAMP1 immunostaining (Figure 3T–U) [48]. When using LysoTracker, traditional statistical analyses can be performed to determine the area and numbers of lysosomes. When applying LAMP1 staining, the area cannot be as reliably obtained, but the relative intensity can provide an estimation of LAMP1 expression in lysosomes, which correlates with the number and size of active lysosomes (Figure 3V). Additionally, other metrics, including length and sphericity, can be determined when using these fluorescent dyes, which suggested that lysosomal dysfunction occurred as length increased and sphericity decreased (Figure 2W–X).

DRP-1 ablation results in increased lipid droplets

We also measured LDs in skeletal muscle from DRP-1smKO mice, which demonstrated a significant increase in LDs compared with the wild-type control (Figure 4A–B, red arrows). We observed a large increase in the lipid area per square micron and the number of lipids per square micron (Figure 4C–D). The increase in LDs was larger, based on the change in percentage, than the observed increases in both lysosomal and autophagosomal structures following DRP-1 ablation (Figures 3 and 4). Increased LDs have previously been described as a downstream effect of autophagy, which supports the conclusion that autophagy increased in frequency following DRP-1 ablation [18]. We propose that this increase in autophagic activity may be due to dysfunctional regulation of mitochondria length, which has previously been demonstrated in response to the loss of DRP-1 regulated fission [18,46]. These results suggest that DRP-1 ablation and the resulting lack of mitochondrial fission increase autophagy in cells, demonstrated by the upregulation of the

cellular degradation machinery. Past studies have found that mice lacking DRP-1 are associated with the increased accumulation of damaged mitochondria [47], which may induce increased mitophagy and thereby induce the relevant recycling machinery.

Knockdown of Marf resulted in more abundant lysosomes

In addition to DRP-1, we sought the quantify changes in lysosomes in response to the knockdown of other key mitochondrial proteins. Mfn2 is an important regulator of mitochondrial fusion [49,50]. Previous studies have shown that Mfn2 deficiency is associated with disrupted ER morphology and mitochondria–ER contacts, resulting in dysfunctional calcium signaling pathways [49,50]. Furthermore, loss of Mfn2 has recently been shown to influence autophagic pathways [49–52]. Specifically, loss of Mfn2 has been shown to stall autophagy at the lysosome and autophagosome stage, causing a buildup in both autophagosomes and lysosomes, by inhibiting their fusion [52]. The *Drosophila* homolog of Mfn2 is Marf, and previous research examining the knockout of genes upstream of Marf demonstrated downstream effects on autophagy [51]. Given this emerging link between autophagy and Marf/Mfn2, we examined the effects of Marf knockdown in *Drosophila* tissue. Marf knockdown resulted in a significant and large increase in lysosome number compared with the wild-type control (Figure 5A–B, D). Additionally, we observed an increase in the average lysosomal area (Figure 5C). These findings indicate a potential upregulation in autophagy, which may represent an autophagic response to ER and mitochondrial stress caused by the loss of Marf [49–52]. Further research highlighting changes in other cellular degradation machinery following the loss of Mfn2/Marf could better elucidate the effects of Mfn2/Marf on the autophagic pathway.

DISCUSSION:

The method described here involves measuring organelles in each image or image quadrant by defining the area of interest using digital tools, which differ from the often-used method of point counting. Point counting can be used to determine the cellular area by overlaying a grid over the cellular area and quantifying the distance between the gridlines and the number of grid intersections, or points, within the cell. The cellular area may then be estimated using the equation $P \times d^2$, where p represents the number of points and d represents the grid distance [26]. Smaller grids can be used to repeat the process for the estimation of organellar area, and these two values can then be utilized to determine the percentage coverage of organelles. Past studies have used point counting to successfully streamline the process of calculating organelle coverage; however, the outcomes of point counting are estimations [26]. Even when the grid distances are smaller, which can increase the accuracy of the calculation, this measurement includes some level of estimation. The method we described uses ImageJ to calculate a more exact area for the structures. Although this process is more time-consuming, the results are highly reproducible, and high-quality data is generated that may be further analyzed using ImageJ. Both forms of analysis remain driven by human evaluation and require the proper identification of the recycling machinery in question. Both point counting and ImageJ-based measurement techniques are viable methods for measuring the frequency of recycling or other types of organelles; however, we view the more accurate measurements associated with ImageJ analysis to be worth the potential increase in time commitment [23,24].

Another consideration is the magnification and the scope of cellular degradation machinery components that are considered in these analyses. Significant heterogeneity in sizes can be observed among components of the degradation machinery, even within the same classification group, which can vary in proportion to the amount of cargo they may hold (Figure 1). The various

organelle types may require different magnification levels to obtain the necessary dimensions when performing TEM imaging (Supplemental Figure 1). Additionally, when deciding which types of recycling machinery should be evaluated, the purpose of the analysis should be considered, and relevant statistical analyses should be applied to obtain appropriate results (Supplemental Figure 1). For example, the total number of LDs may not be as impactful as their total cell coverage due to the varying sizes of LDs. Therefore, proper magnification should be determined in relation to the necessary measurements that must be performed (Supplemental Figure 1). One limitation of our method is that for key measurements, such as area, the total organelle should be visualized to obtain the most reliable results. Point counting can be used to evaluate images in which the entire organelle is not visible because it relies on estimation [26]. However, when using ImageJ, the entire organelle is outlined, and magnification that is too high may limit the amount of data that can be collected. However, images of a single cell at varying magnifications may be used by normalizing against the same scale across all images.

Although this protocol focuses primarily on the evaluation of the degradation machinery, these organelles must not be viewed in a vacuum. Autophagy can target any cell, and various factors can alter the autophagy rate in various cells, as exemplified by changes in cancer, metabolic diseases or neurodegenerative diseases [1,4,9]. Many organelles are closely associated with the overall process of autophagy. Recent research has found that omegasomes and autophagosomes primarily form at mitochondria–ER contact sites [25], which may be associated with the necessity of phosphatidylinositol 3-phosphate, an ER phospholipid, for the activation and formation of autophagosomes [1–3]. Tangentially, research has also found that mitochondrial-derived vesicles can factor into autophagic pathways by transporting proteins and lipids associated with the mitochondria to MVBs [53]. This previously unknown pathway

indicates that mitochondria that are not sufficiently damaged to undergo mitophagy can still produce endocytic bundles that are transported to the MVB for recycling via the autophagic pathway. Cellular degradation machinery can have important effects on organelles, and the inverse is also true. To properly study autophagy, a holistic view should be applied with respect to cellular organelles to better understand the nuances that influence autophagy.

The protocol described here is optimal for the performance of various statistical analyses; however, a primary concern is ensuring that the correct subcellular features of lysosomes, autophagosomes, and LDs are identified and measured. Although organelles can be accurately identified using TEM analysis alone, the use of additional methods, such as immunofluorescent staining, is recommended in tandem with TEM analysis. Clear and useful results can be obtained from complementary methods, particularly when analyzing lysosomes, autophagosomes, and autolysosomes, which can easily be misidentified (Figures 1 and 3). Examining organellar morphology using TEM alone may not be sufficient and could lead to inaccurate conclusions. Thus, to verify and validate the correct identification of each organellar structure, we propose that other methods should be performed in tandem with TEM, such as immuno-TEM with gold labeling, LysoTracker with an overlay of correlative light and electron microscopy, and immunohistochemistry or immunofluorescence (Figure 1 and 3) [5,41,54].

Given the acidity and multitude of proteins associated with lysosomes, various avenues are available for the identification of lysosomes through immunogold labeling, LysoTracker to identify acidic organelles, and the use of immunofluorescent dyes to label lysosome-associated proteins or indirect immunofluorescence through the use of secondary antibodies bound to primary antibody associated with lysosomes [55]. For example, past studies have utilized the staining of LAMP1 to detect lysosomes (Figure 3T–U) [48]. When combining confocal fluorescence imaging

and TEM, fluorescence can be used to identify the presence of specific proteins and confirm the identities of autophagic organelles (Figure 3O–X), and TEM can then be used to measure the finer details, including area, average number, and percent coverage (Figure 3A–N). Increased noise and decreased ultrastructural details may be observed when buffer is utilized with these techniques; therefore, sample additives should be minimized, and immunofluorescent dyes should only be used when necessary [56].

Current options are limited for the identification and classification of autophagosomes. Immunogold labeling can be utilized against LC3-II, which is currently the standard and only known autophagosomal marker [41,54,57]. LC3 puncta may not always be detectable in autophagosomes; however, the application of immunogold labeling can be effectively applied for the identification of organelles that should be excluded from the analysis of autophagosomes. For example, CAV-1 staining (Figure 1S–T), which is associated with caveolae typically found in MVBs, can be used to identify MVBs that might be mistaken for autophagosomes (Figure 1H) [44]. Similarly, perilipin 2, which is a commonly expressed protein associated principally with LDs, can be used for the identification of LDs [58]. Future studies that continue to explore new avenues for better immunogold or immunofluorescence labeling options for autophagosomes are also important. Due to the potential ambiguity associated with identifying the cellular degradation machinery, we recommend the use of at least one additional complementary technique for the verification of lysosome and autophagosome identification when measuring TEM images.

Although limitations exist for this TEM analysis method, when combined with other techniques, the reliable identification and quantification of cellular degradation machinery components may be possible. On a broader scale, this basic method utilizing ImageJ may be applied to many fields of study with a focus on organelle structure. For example, mitochondria

have been shown to play key roles in many complex diseases, including type II diabetes, cardiomyopathy, and Alzheimer's disease [21,22,37–40]. Additionally, autophagy may play a role in these diseases, given its role in mediating mitophagy to clear dysfunctional mitochondria. The use of TEM and ImageJ to study other organelles in conjunction with the precise methodology outlined here for the study of key autophagic organelles will lead to a better understanding of the physiology associated with other key organelles and their contributions to disease.

PERSPECTIVES ON STAINING:

Various lysosome stages may look different when using different EM staining procedures. Lysosomes will present differently depending on the material used for preparation (e.g., osmium or osmium tetroxide) and the type and amount of additives used (e.g., uranyl acetate, lead citrate, and ruthenium red). Depending on the stain used, contrasts of the lysosomal membranes may be altered, changing how lysosome-related structures appear. All EM images shown here used a grid-based staining technique that is used across all procedures (Table 2). The general TEM sample preparation protocol used glutaraldehyde and 1% osmium tetroxide as fixatives [59–62]. From there, post staining on TEM ultrathin sections utilized 5% Uranyl Acetate (UA) for 6 min and Reynold's Lead Citrate for 3 min [63–65]. These are commonly used reagents for staining; UA can increase membrane contrast and lead citrate can improve resolution of cellular structures. Different stains can be used to better suit the purpose of the experiment being performed, and application length of stains should be adjusted accordingly to the sample type. Other viable alternatives exist; for example, ruthenium tetroxide may be used, especially for the preparation of kidney, liver, and prostate tissue [66,67]. Ammoniated ruthenium oxychloride, commonly referred to as ruthenium red, is also frequently used as a

polycationic dye to stain negatively charged molecular species, including polysaccharides, in tissue sections [68–70]. Although ruthenium red is commonly used for fungal staining, when used in tandem with osmium tetroxide, a chemical reaction happens that may increase contrast of TEM micrographs [68–70]. Regardless of the stain used, the foremost concern should be remaining consistent in staining tissues. Different staining in the same organism, for example staining separately for lysosomes, should be avoided. Ideally, the same staining solution should be used for all samples, even different stages, this way it is possible to compare between different time or stages. However, if staining protocols used are different than the ones laid out here due to adjustments being made, appearances of lysosomes may vary.

ACKNOWLEDGMENTS:

We also would like to thank our undergraduate colleagues Benjamin Kirk and Innes Hicsasmaz for assisting with the optimization of this analysis technique. This work was supported by NIH grants, R01HL108379 and R01DK092065 to E.D.A; T32 HL007121, the UNCF/BMS EE Just Faculty Fund, the Burroughs Welcome Fund CASI Award, the Ford Foundation, NIH SRP subaward to #5R25HL106365-12 from the NIH PRIDE Program to AHJ; and NSF MCB #2011577I to S.A.M; 2U54CA 1633069-07 from NCI and R25 GM059994/GM/NIHGMS NIH to H.K.B.

DISCLOSURES:

The authors have no disclosures to report.

REFERENCES:

1. Ryter, S.W.; Bhatia, D.; Choi, M.E. Autophagy: A Lysosome-Dependent Process with Implications in Cellular Redox Homeostasis and Human Disease. *Antioxidants & redox signaling* **2019**, *30*, 138–159.
2. Yin, Z.; Pascual, C.; Klionsky, D.J. Autophagy: Machinery and Regulation. *Microbial cell* **2016**, *3*, 588.
3. Levy, J.M.M.; Thorburn, A. Autophagy in Cancer: Moving from Understanding Mechanism to Improving Therapy Responses in Patients. *Cell Death & Differentiation* **2020**, *27*, 843–857.
4. Eskelinen, E.-L. Maturation of Autophagic Vacuoles in Mammalian Cells. *Autophagy* **2005**, *1*, 1–10.
5. Bernard, A.; Klionsky, D.J. Autophagosome Formation: Tracing the Source. *Developmental cell* **2013**, *25*, 116–117.
6. Yu, L.; Chen, Y.; Tooze, S.A. Autophagy Pathway: Cellular and Molecular Mechanisms. *Autophagy* **2018**, *14*, 207–215.
7. Jung, M.; Choi, H.; Mun, J.Y. The Autophagy Research in Electron Microscopy. *Applied Microscopy* **2019**, *49*, 1–7.
8. Lam, J.; Katti, P.; Biete, M.; Mungai, M.; AshShareef, S.; Neikirk, K.; Lopez, E.G.; Vue, Z.; Christensen, T.A.; Beasley, H.K. A Universal Approach to Analyzing Transmission Electron Microscopy with ImageJ. *bioRxiv* **2021**.
9. Eskelinen, E.-L.; Reggiori, F.; Baba, M.; Kovács, A.L.; Seglen, P.O. Seeing Is Believing: The Impact of Electron Microscopy on Autophagy Research. *Autophagy* **2011**, *7*, 935–956.
10. Rasband, W.S. Imagej, Us National Institutes of Health, Bethesda, Maryland, Usa. *http://imagej. nih. gov/ij/* **2011**.
11. Trivedi, P.C.; Bartlett, J.J.; Pulinilkunnil, T. Lysosomal Biology and Function: Modern View of Cellular Debris Bin. *Cells* **2020**, *9*, 1131.
12. Heuser, J. Changes in Lysosome Shape and Distribution Correlated with Changes in Cytoplasmic PH. *Journal of Cell Biology* **1989**, *108*, 855–864.
13. Cuervo, A.M.; Dice, J.F. When Lysosomes Get Old☆. *Experimental gerontology* **2000**, *35*, 119–131.
14. Talsma, H.; Jousma, H.; Nicolay, K.; Crommelin, D. Multilamellar or Multivesicular Vesicles? *International journal of pharmaceutics* **1987**, *37*, 171–173.
15. Eskelinen, E.-L. To Be or Not to Be? Examples of Incorrect Identification of Autophagic Compartments in Conventional Transmission Electron Microscopy of Mammalian Cells. *Autophagy* **2008**, *4*, 257–260.
16. Cui, Y.; He, Y.; Cao, W.; Gao, J.; Jiang, L. The Multivesicular Body and Autophagosome Pathways in Plants. *Frontiers in plant science* **2018**, *9*, 1837.
17. Fader, C.; Colombo, M. Autophagy and Multivesicular Bodies: Two Closely Related Partners. *Cell Death & Differentiation* **2009**, *16*, 70–78.
18. Nguyen, T.B.; Olzmann, J.A. Lipid Droplets and Lipotoxicity during Autophagy. *Autophagy* **2017**, *13*, 2002–2003.
19. Olzmann, J.A.; Carvalho, P. Dynamics and Functions of Lipid Droplets. *Nature reviews Molecular cell biology* **2019**, *20*, 137–155.
20. Qi, Z.; Chen, L. Endoplasmic Reticulum Stress and Autophagy. *Autophagy: Biology and Diseases* **2019**, 167–177.

21. Eura, Y.; Ishihara, N.; Yokota, S.; Mihara, K. Two Mitofusin Proteins, Mammalian Homologues of FZO, with Distinct Functions Are Both Required for Mitochondrial Fusion. *Journal of biochemistry* **2003**, *134*, 333–344.
22. Hales, K.G.; Fuller, M.T. Developmentally Regulated Mitochondrial Fusion Mediated by a Conserved, Novel, Predicted GTPase. *Cell* **1997**, *90*, 121–129.
23. Kim, S.; Choi, S.; Kang, D. Quantitative and Qualitative Analysis of Autophagy Flux Using Imaging. *BMB reports* **2020**, *53*, 241.
24. Arai, R.; Waguri, S. Improved electron microscopy fixation methods for tracking autophagy-associated membranes in cultured mammalian cells. In *Autophagy*; Springer, 2019; pp. 211–221.
25. Hamasaki, M.; Furuta, N.; Matsuda, A.; Nezu, A.; Yamamoto, A.; Fujita, N.; Oomori, H.; Noda, T.; Haraguchi, T.; Hiraoka, Y. Autophagosomes Form at ER–Mitochondria Contact Sites. *Nature* **2013**, *495*, 389–393.
26. Ylä-Anttila, P.; Vihinen, H.; Jokitalo, E.; Eskelinen, E. Monitoring Autophagy by Electron Microscopy in Mammalian Cells. *Methods in enzymology* **2009**, *452*, 143–164.
27. Pereira, R.O.; Tadinada, S.M.; Zasadny, F.M.; Oliveira, K.J.; Pires, K.M.P.; Olvera, A.; Jeffers, J.; Souvenir, R.; Mcglauflin, R.; Seei, A. OPA 1 Deficiency Promotes Secretion of FGF 21 from Muscle That Prevents Obesity and Insulin Resistance. *The EMBO journal* **2017**, *36*, 2126–2145.
28. Southard, S.; Low, S.; Li, L.; Rozo, M.; Harvey, T.; Fan, C.; Lepper, C. A Series of Cre-ERT2 Drivers for Manipulation of the Skeletal Muscle Lineage. *genesis* **2014**, *52*, 759–770.
29. Favaro, G.; Romanello, V.; Varanita, T.; Desbats, M.A.; Morbidoni, V.; Tezze, C.; Albiero, M.; Canato, M.; Gherardi, G.; De Stefani, D. DRP1-Mediated Mitochondrial Shape Controls Calcium Homeostasis and Muscle Mass. *Nature communications* **2019**, *10*, 1–17.
30. Katti, P.; Rai, M.; Srivastava, S.; Nongthomba, U. Marf-Mediated Mitochondrial Fusion Is Imperative for the Development and Functioning of Indirect Flight Muscles (IFMs) in Drosophila. *Experimental Cell Research* **2021**, *399*, 112486.
31. Han, J.; Back, S.H.; Hur, J.; Lin, Y.-H.; Gildersleeve, R.; Shan, J.; Yuan, C.L.; Krokowski, D.; Wang, S.; Hatzoglou, M. ER-Stress-Induced Transcriptional Regulation Increases Protein Synthesis Leading to Cell Death. *Nature cell biology* **2013**, *15*, 481–490.
32. Galmes, R.; Houcine, A.; van Vliet, A.R.; Agostinis, P.; Jackson, C.L.; Giordano, F. ORP5/ORP8 Localize to Endoplasmic Reticulum–Mitochondria Contacts and Are Involved in Mitochondrial Function. *EMBO reports* **2016**, *17*, 800–810.
33. Chazotte, B. Labeling Lysosomes in Live Cells with LysoTracker. *Cold Spring Harbor Protocols* **2011**, *2011*, pdb-prot5571.
34. Delrue, R.; Martinez-Lorenzo, M.; Lestrate, P.; Danese, I.; Bielarz, V.; Mertens, P.; De Bolle, X.; Tibor, A.; Gorvel, J.; Letesson, J. Identification of Brucella Spp. Genes Involved in Intracellular Trafficking. *Cellular microbiology* **2001**, *3*, 487–497.
35. Parra, V.; Verdejo, H.E.; Iglewski, M.; Del Campo, A.; Troncoso, R.; Jones, D.; Zhu, Y.; Kuzmicic, J.; Pennanen, C.; Lopez-Crisosto, C. Insulin Stimulates Mitochondrial Fusion and Function in Cardiomyocytes via the Akt-MTOR-NFκB-Opa-1 Signaling Pathway. *Diabetes* **2014**, *63*, 75–88.
36. Pasqua, T.; Mahata, S.; Bandyopadhyay, G.K.; Biswas, A.; Perkins, G.A.; Sinha-Hikim, A.P.; Goldstein, D.S.; Eiden, L.E.; Mahata, S.K. Impact of Chromogranin A Deficiency on Catecholamine Storage, Catecholamine Granule Morphology and Chromaffin Cell Energy Metabolism in Vivo. *Cell and tissue research* **2016**, *363*, 693–712.

37. Mozdy, A.D.; Shaw, J.M. A Fuzzy Mitochondrial Fusion Apparatus Comes into Focus. *Nature reviews Molecular cell biology* **2003**, *4*, 468–478.
38. Rojo, M.; Legros, F.; Chateau, D.; Lombès, A. Membrane Topology and Mitochondrial Targeting of Mitofusins, Ubiquitous Mammalian Homologs of the Transmembrane GTPase Fzo. *Journal of cell science* **2002**, *115*, 1663–1674.
39. Santel, A.; Fuller, M.T. Control of Mitochondrial Morphology by a Human Mitofusin. *Journal of cell science* **2001**, *114*, 867–874.
40. Santel, A.; Frank, S.; Gaume, B.; Herrler, M.; Youle, R.J.; Fuller, M.T. Mitofusin-1 Protein Is a Generally Expressed Mediator of Mitochondrial Fusion in Mammalian Cells. *Journal of cell science* **2003**, *116*, 2763–2774.
41. Klionsky, D.J.; Abeliovich, H.; Agostinis, P.; Agrawal, D.K.; Aliev, G.; Askew, D.S.; Baba, M.; Baehrecke, E.H.; Bahr, B.A.; Ballabio, A. Guidelines for the Use and Interpretation of Assays for Monitoring Autophagy in Higher Eukaryotes. *Autophagy* **2008**, *4*, 151–175.
42. Kabeya, Y.; Mizushima, N.; Ueno, T.; Yamamoto, A.; Kirisako, T.; Noda, T.; Kominami, E.; Ohsumi, Y.; Yoshimori, T. LC3, a Mammalian Homologue of Yeast Apg8p, Is Localized in Autophagosome Membranes after Processing. *The EMBO journal* **2000**, *19*, 5720–5728.
43. Jager, S.; Bucci, C.; Tanida, I.; Ueno, T.; Kominami, E.; Saftig, P.; Eskelinen, E.-L. Role for Rab7 in Maturation of Late Autophagic Vacuoles. *Journal of cell science* **2004**, *117*, 4837–4848.
44. Botos, E.; Klumperman, J.; Oorschot, V.; Igyarto, B.; Magyar, A.; Oláh, M.; Kiss, A. Caveolin-1 Is Transported to Multi-vesicular Bodies after Albumin-induced Endocytosis of Caveolae in HepG2 Cells. *Journal of cellular and molecular medicine* **2008**, *12*, 1632–1639.
45. Lindner, P.; Christensen, S.B.; Nissen, P.; Møller, J.V.; Engedal, N. Cell Death Induced by the ER Stressor Thapsigargin Involves Death Receptor 5, a Non-Autophagic Function of MAP1LC3B, and Distinct Contributions from Unfolded Protein Response Components. *Cell Communication and Signaling* **2020**, *18*, 1–23.
46. Ikeda, Y.; Shirakabe, A.; Maejima, Y.; Zhai, P.; Sciarretta, S.; Toli, J.; Nomura, M.; Mihara, K.; Egashira, K.; Ohishi, M. Endogenous Drp1 Mediates Mitochondrial Autophagy and Protects the Heart against Energy Stress. *Circulation research* **2015**, *116*, 264–278.
47. Zuo, W.; Zhang, S.; Xia, C.-Y.; Guo, X.-F.; He, W.-B.; Chen, N.-H. Mitochondria Autophagy Is Induced after Hypoxic/Ischemic Stress in a Drp1 Dependent Manner: The Role of Inhibition of Drp1 in Ischemic Brain Damage. *Neuropharmacology* **2014**, *86*, 103–115.
48. Cheng, X.-T.; Xie, Y.-X.; Zhou, B.; Huang, N.; Farfel-Becker, T.; Sheng, Z.-H. Revisiting LAMP1 as a Marker for Degradative Autophagy-Lysosomal Organelles in the Nervous System. *Autophagy* **2018**, *14*, 1472–1474.
49. Casellas-Díaz, S.; Larramona-Arcas, R.; Riqué-Pujol, G.; Tena-Morraja, P.; Müller-Sánchez, C.; Segarra-Mondejar, M.; Gavaldà-Navarro, A.; Villarroya, F.; Reina, M.; Martínez-Estrada, O.M. Mfn2 Localization in the ER Is Necessary for Its Bioenergetic Function and Neuritic Development. *EMBO reports* **2021**, e51954.
50. Muñoz, J.P.; Ivanova, S.; Sánchez-Wandelmer, J.; Martínez-Cristóbal, P.; Noguera, E.; Sancho, A.; Díaz-Ramos, A.; Hernández-Alvarez, M.I.; Sebastián, D.; Mauvezin, C. Mfn2

Modulates the UPR and Mitochondrial Function via Repression of PERK. *The EMBO journal* **2013**, *32*, 2348–2361.

51. Shen, J.L.; Fortier, T.M.; Zhao, Y.G.; Wang, R.; Burmeister, M.; Baehrecke, E.H. Vmp1, Vps13D, and Marf/Mfn2 Function in a Conserved Pathway to Regulate Mitochondria and ER Contact in Development and Disease. *Current Biology* **2021**.
52. Zhao, T.; Huang, X.; Han, L.; Wang, X.; Cheng, H.; Zhao, Y.; Chen, Q.; Chen, J.; Cheng, H.; Xiao, R. Central Role of Mitofusin 2 in Autophagosome-Lysosome Fusion in Cardiomyocytes. *Journal of Biological Chemistry* **2012**, *287*, 23615–23625.
53. Sugiura, A.; McLelland, G.; Fon, E.A.; McBride, H.M. A New Pathway for Mitochondrial Quality Control: Mitochondrial-derived Vesicles. *The EMBO journal* **2014**, *33*, 2142–2156.
54. Martinet, W.; Timmermans, J.-P.; De Meyer, G.R. Methods to Assess Autophagy in Situ—Transmission Electron Microscopy versus Immunohistochemistry. *Methods in enzymology* **2014**, *543*, 89–114.
55. Allaire, A.; Picard-Jean, F.; Bisaillon, M. Immunofluorescence to Monitor the Cellular Uptake of Human Lactoferrin and Its Associated Antiviral Activity against the Hepatitis C Virus. *Journal of visualized experiments: JoVE* **2015**.
56. Odell, I.D.; Cook, D. Immunofluorescence Techniques. *The Journal of investigative dermatology* **2013**, *133*, e4.
57. Nair, U.; Yen, W.-L.; Mari, M.; Cao, Y.; Xie, Z.; Baba, M.; Reggiori, F.; Klionsky, D.J. A Role for Atg8–PE Deconjugation in Autophagosome Biogenesis. *Autophagy* **2012**, *8*, 780–793.
58. Listenberger, L.L.; Studer, A.M.; Brown, D.A.; Wolins, N.E. Fluorescent Detection of Lipid Droplets and Associated Proteins. *Current Protocols in Cell Biology* **2016**, *71*, 4–31.
59. Franke, W.; Krien, S.; Brown Jr, R. Simultaneous Glutaraldehyde-Osmium Tetroxide Fixation With Postosmication. An Improved Fixation Procedure for Electron Microscopy of Plant and Animal Cells. *Histochemie. Histochemistry. Histochimie* **1969**, *19*, 162–164.
60. Porter, K.; Kallman, F. The Properties and Effects of Osmium Tetroxide as a Tissue Fixative with Special Reference to Its Use for Electron Microscopy. *Experimental Cell Research* **1953**, *4*, 127–141.
61. Cope, G.; Williams, M. Quantitative Studies on the Preservation of Choline and Ethanolamine Phosphatides during Tissue Preparation for Electron Microscopy: I. Glutaraldehyde, Osmium Tetroxide, Araldite Methods. *Journal of microscopy* **1969**, *90*, 31–46.
62. White, D.; Mazurkiewicz, J.; Barrnett, R. A Chemical Mechanism for Tissue Staining by Osmium Tetroxide-Ferrocyanide Mixtures. *Journal of Histochemistry & Cytochemistry* **1979**, *27*, 1084–1091.
63. Venable, J.H.; Coggeshall, R. A Simplified Lead Citrate Stain for Use in Electron Microscopy. *The Journal of cell biology* **1965**, *25*, 407–408.
64. Derksen, J.; Meekes, H. Selective Staining of Nucleic Acid Containing Structures by Uranyl Acetate-Lead Citrate. *Micron and microscopica acta* **1984**, *15*, 55–58.
65. Yamaguchi, M.; Shimizu, M.; Yamaguchi, T.; Ohkusu, M.; Kawamoto, S. Repeated Use of Uranyl Acetate Solution in Section Stainingin Transmission Electron Microscopy. *Plant Morphology* **2005**, *17*, 57–59.
66. Gaylarde, P.; Sarkany, I. Ruthenium Tetroxide for Fixing and Staining Cytoplasmic Membranes. *Science* **1968**, *161*, 1157–1158.
67. Headquarters, U.C. Ruthenium Tetroxide.

68. Linss, W.; Kiss, A.; Geyer, G. A Ruthenium Red-Osmium Tetroxide Section Staining Method (Author's Transl). *Acta histochemica* **1979**, *64*, 206–212.
69. Dierichs, R. Ruthenium Red as a Stain for Electron Microscopy. Some New Aspects of Its Application and Mode of Action. *Histochemistry* **1979**, *64*, 171–187.
70. McKay, A. A Plate Assay Method for the Detection of Fungal Polygalacturonase Secretion. *FEMS Microbiology letters* **1988**, *56*, 355–358.

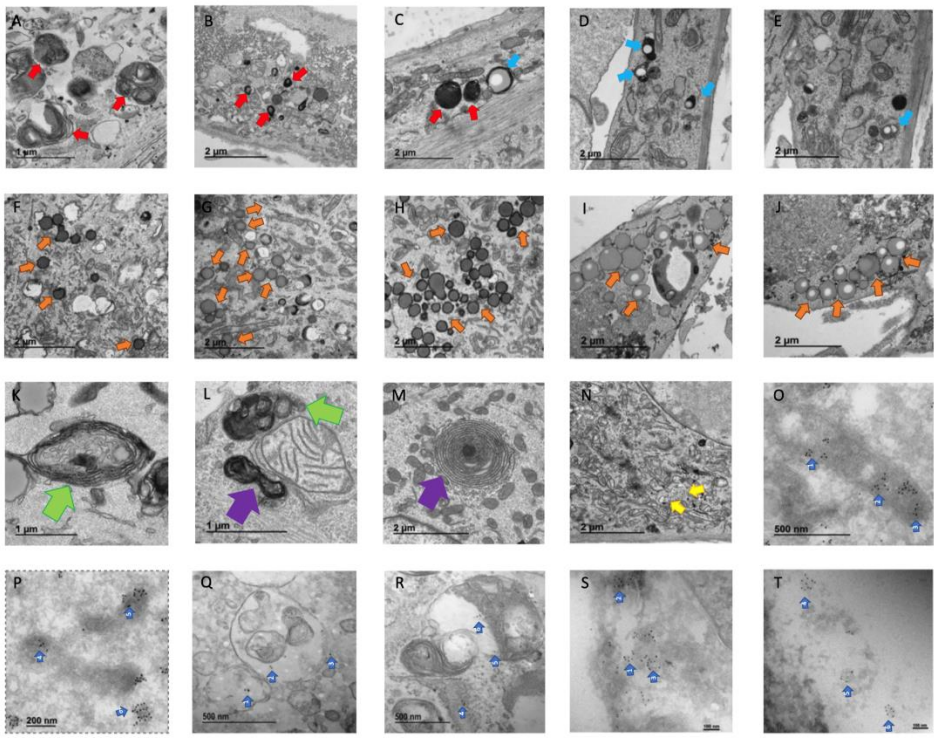

Figure 1. Identification of lysosomes, autolysosomes, lipid droplets, multilamellar vesicular bodies, autophagosomes, inclusion bodies, mitochondria, and lipid droplets using TEM and immunogold labeling. (A-N) Red arrows show lysosomes, yellow arrows show multivesicular inclusion bodies, green arrows show varying autophagosomes, orange arrows show lipid droplets, purple arrows show multilamellar vesicular bodies, and blue arrows show autolysosomes. (**O–T**) Immunogold labeling using mitofusin 1 (MFN-1), microtubule-associated protein 1 light chain 3 (LC3), and caveolin 1 (CAV-1) to identify mitochondria. (**O and P**) Several representative images of mitochondria featuring MFN-1 immunogold labeling. In mitochondria, MFN-1 can be identified by black dots as MFN-1 puncta. (**O.1–3, blue arrows**) MFN-1 is not always consistently expressed throughout the mitochondria but will be evident in most mitochondria, especially at lower magnifications. (**P.4–6, blue arrows**) In mitochondria undergoing fusion, or having recently undergone fusion, an increased number of MFN-1-positive puncta will be visible. (**Q and R**) Several representative images of autophagosomes identified using LC3 immunogold labeling. In autophagosomes, LC3 presence can be identified by black dots as LC3 puncta. Unlike many other forms of immunogold labeling, LC3 puncta do not have a consistent appearance. As a result, as identified by the blue arrows, they may appear as (**Q.1, left arrow**) clusters of thick puncta, (**Q.2, middle arrow**) internal puncta, (**Q.3, right arrow**) proximal to the membrane, (**R.4, left arrow**) faded and clustered, (**R.5, middle arrow**) alone and faded, or (**R.6, right arrow**) in varying sizes. This diversity of puncta can still pose challenges to the identification of autophagosomes using immunogold labeling. CAV-1 can be used to identify vesicles, including multivesicular bodies, which are easily mistaken for autophagosomes. (**S and T**) CAV-1 positive puncta can be difficult to identify in lower-magnification images and may blend in with the background. (**S.1–3, blue arrows**) Many vesicles will have multiple puncta rather than a singular punctum. (**T.4–6, blue arrows**) CAV-1-positive puncta cluster around the membrane and inside of multivesicular bodies.

The presence of CAV-1 puncta indicates that these organelles are not autophagosomes or lysosomes.

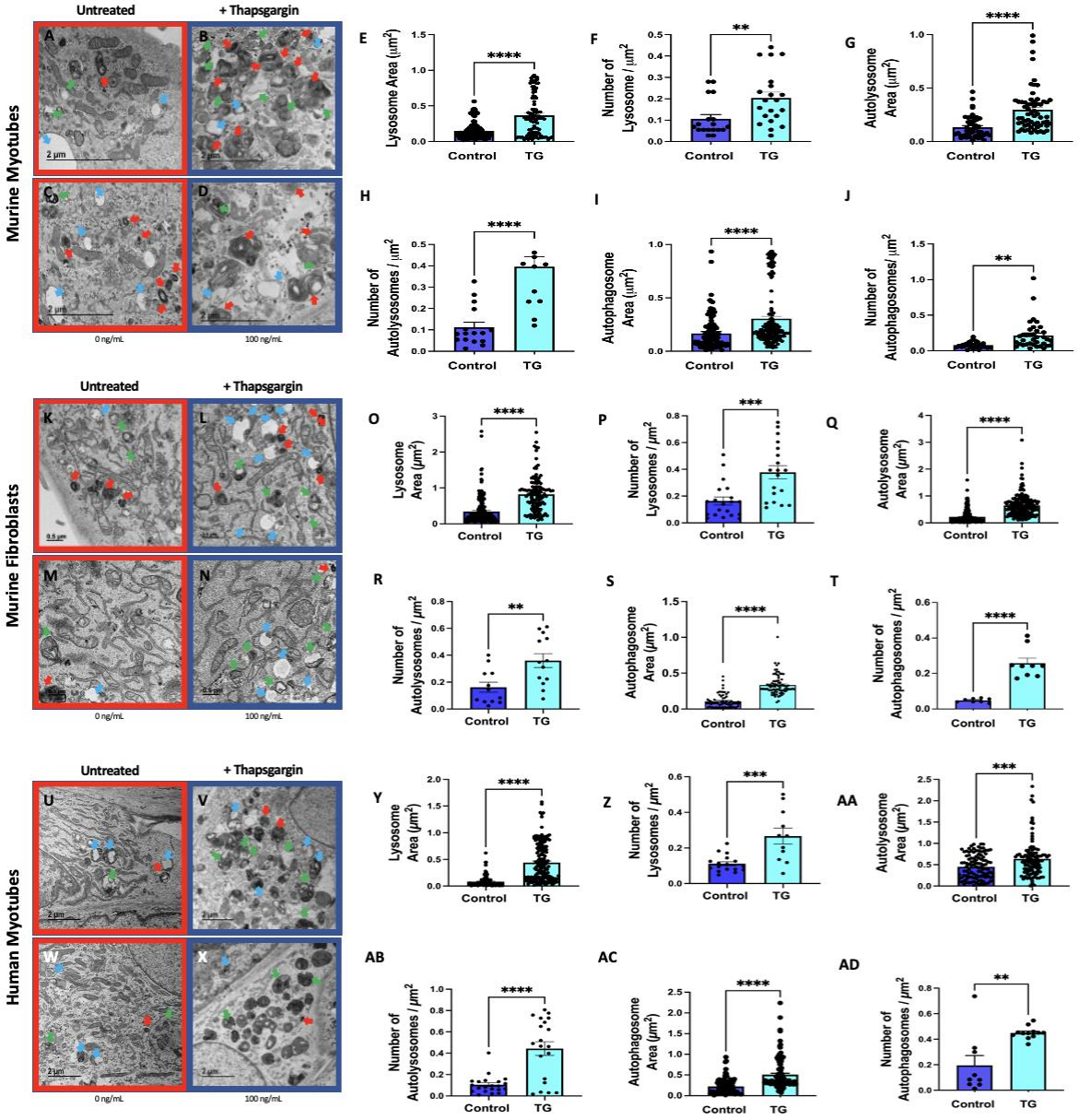

Figure 2. Thapsigargin alters lysosomal, autolysosomal, and autophagosomal morphologies in primary mouse skeletal myotubes, mouse fibroblasts and human myotubes. (**A–D**) Representative transmission electron microscopy (TEM) images of cellular degradation machinery in skeletal muscle from untreated (red outline) and thapsigargin-treated (blue outline) mouse myotubes. Lysosomes are identified by red arrows, green arrows show autophagosomes, and blue arrows show autolysosomes. (**E**) Quantification of the lysosomal area in each treatment group. (**F**) Quantification of the number of lysosomes per square micron. (**G**) Quantification of the autolysosomal area. (**H**) Quantification of the number of autolysosomes per square micron. (**I**) Quantification of the autophagosomal area in each treatment group. (**J**) Quantification of the number of autophagosomes per square micron. (**K–N**) Representative TEM images of cellular degradation machinery in mouse fibroblasts from

untreated (red outline) and thapsigargin-treated (blue outline) cells. (**O**) Quantification of the lysosomal area in each treatment group. (**P**) Quantification of the number of lysosomes per square micron. (**Q**) Quantification of the autolysosomal area. (**R**) Quantification of the number of autolysosomes per square micron. (**S**) Quantification of the autophagosomal area in each treatment group. (**T**) Quantification of the number of autophagosomes per square micron. (**U–X**) Representative TEM images of cellular degradation machinery in human myotubes from untreated (red outline) and thapsigargin-treated (blue outline) cells. (**Y**) Quantification of the lysosomal area in each treatment group. (**Z**) Quantification of the number of lysosomes per square micron. (**AA**) Quantification of the autolysosomal area. (**AB**) Quantification of the number of autolysosomes per square micron. (**AC**) Quantification of the autophagosomal area in each treatment group. (**AD**) Quantification of the number of autophagosomes per square micron. Significant differences are indicated by asterisks; *, **, ***, **** indicate $p \leq 0.05$, $p \leq 0.01$, $p \leq 0.001$, and $p \leq 0.0001$, respectively.

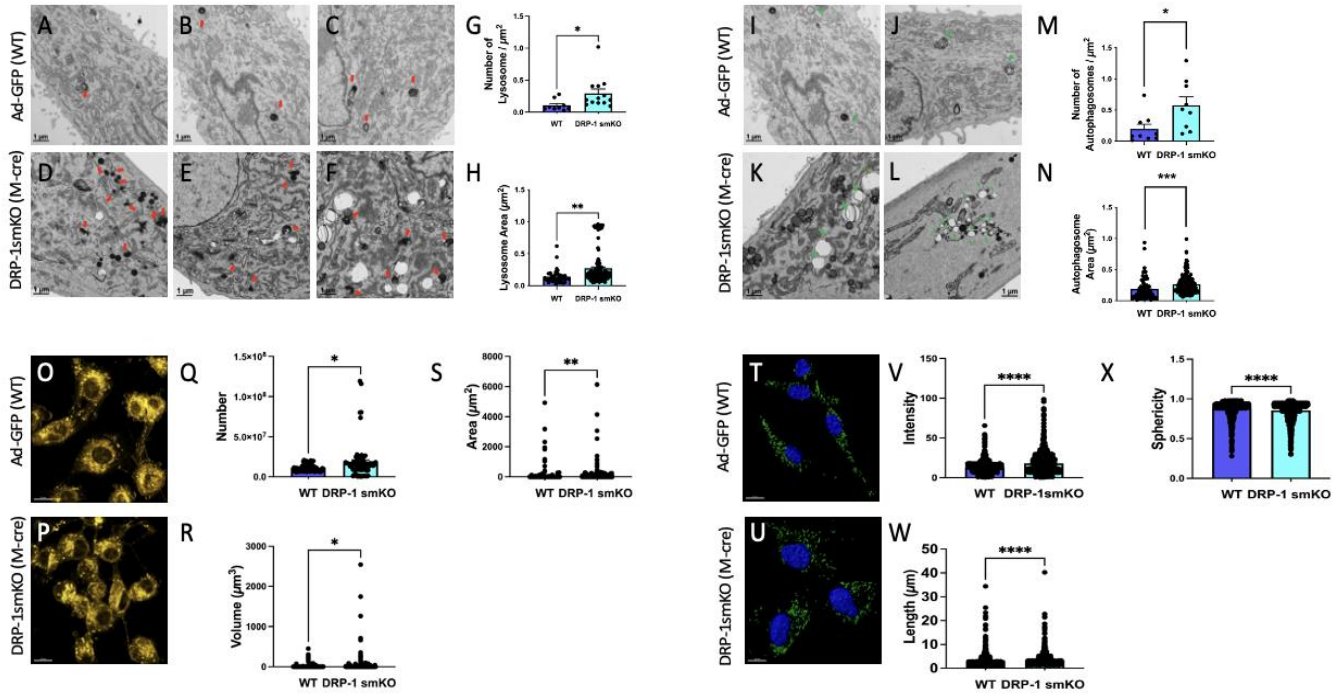

Figure 3. Knockout of dynamin-related protein (DRP-1) increases lysosomes and autophagosomes, as identified through TEM, lysotracker, and lysosome-associated membrane protein (LAMP1). (**A–F**) Representative transmission electron microscopy (TEM) images of skeletal muscle myotubes from DRP-1 knockout (bottom) and wild-type (top) mice. Lysosomes are indicated by the red arrows while green arrows show autophagosomes. (**G**) Quantification of the normalized number of lysosomes per cell micrometer and (**H**) average lysosomal area. (**I–L**) Representative TEM images of skeletal muscle cells from DRP-1 knockout (bottom) and wild-type (top) mice. Autophagosomes are indicated by the red arrows. (**M**) Quantification of the normalized number of autophagosomes per cell micrometer and (**N**) average autophagosomal area. (**O and P**) Representative images of DRP-1 smKO and wild-type (WT) lysosomes with lysotracker applied. (**Q**) The number of lysosomes, (**R**) the average calculated volume, and (**S**) the average area of the lysosomes, all of which increased upon DRP-1 ablation. (**T and U**) Lysosomes can be identified using the immunofluorescent labeling of LAMP1 protein. (**V**) The intensity of the signature LAMP1 blue color can be measured to determine the frequency of active lysosomes in the cell. (**W**) Lysosome dysfunction or changes in morphology can be determined by measuring the length of fluorescence signatures, and (**X**) the sphericity of regions of interest. Significant differences are indicated by asterisks; *, **, ***, **** indicate $p \leq 0.05$, $p \leq 0.01$, $p \leq 0.001$, and $p \leq 0.0001$, respectively.

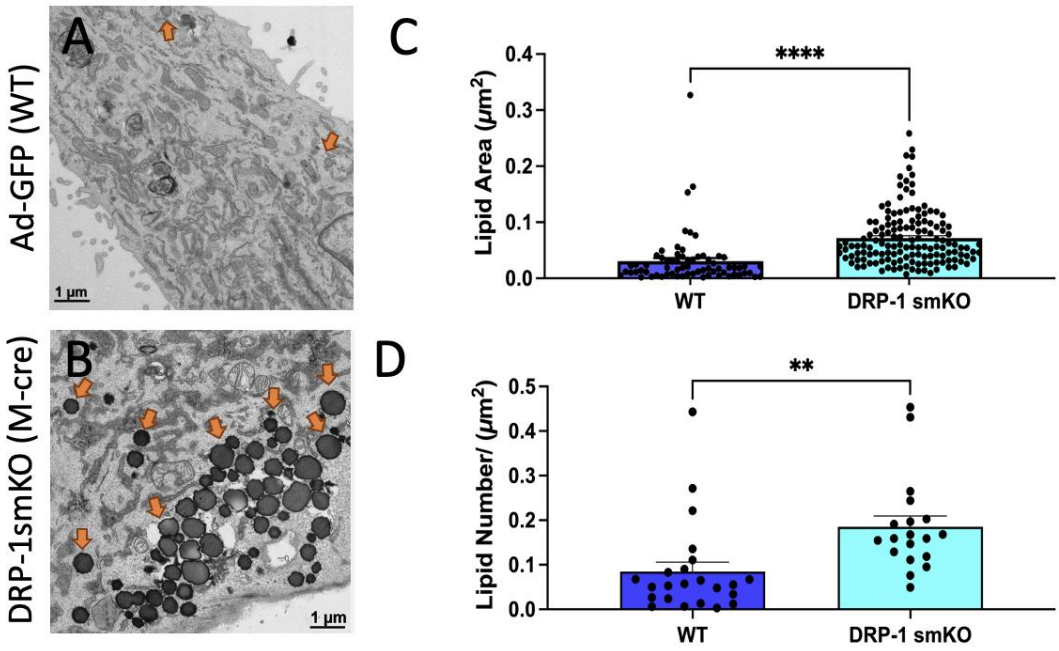

Figure 4. Knockout of dynamin-related protein (DRP-1) increases lipid droplets in mouse skeletal myotubes.

(**A and B**) Representative transmission electron microscopy (TEM) images of skeletal myotubes from DRP-1 knockout (bottom) and wild-type (top) mice. Lipid droplets are indicated by the orange arrows. (**C**) Quantification of the total lipid area and (**D**) the normalized number of lipid droplets per μm^2 of cell area. Significant differences are indicated by asterisks above the respective figures; **, **** indicate $p \leq 0.01$ and $p \leq 0.0001$, respectively.

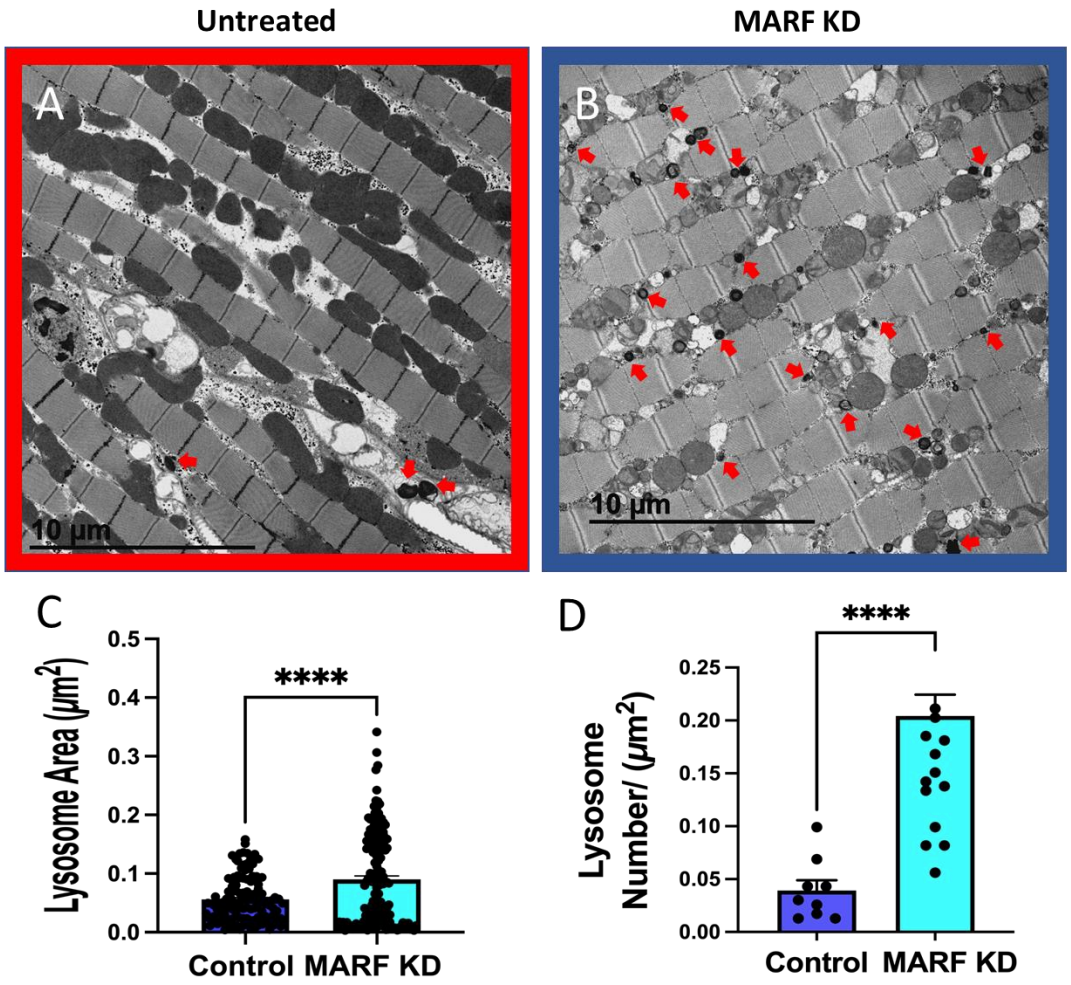

Figure 5. Knockdown of MARF increases lysosome number and average lysosome area.

(**A and B**) Representative transmission electron microscopy (TEM) images of cellular degradation machinery from control (red outline) and mitochondrial assembly regulatory factor (MARF) knockdown (KD; blue outline) in drosophila tissue. Lysosome examples are identified with red arrows. (**C**) Quantification of the normalized number of lysosomes per µm^2 of cell area and (**D**) average lysosomal area. Significant differences are indicated by asterisks above the respective figures; ** and **** indicate $p \leq 0.01$ and $p \leq 0.0001$, respectively.

Supplementary Files:

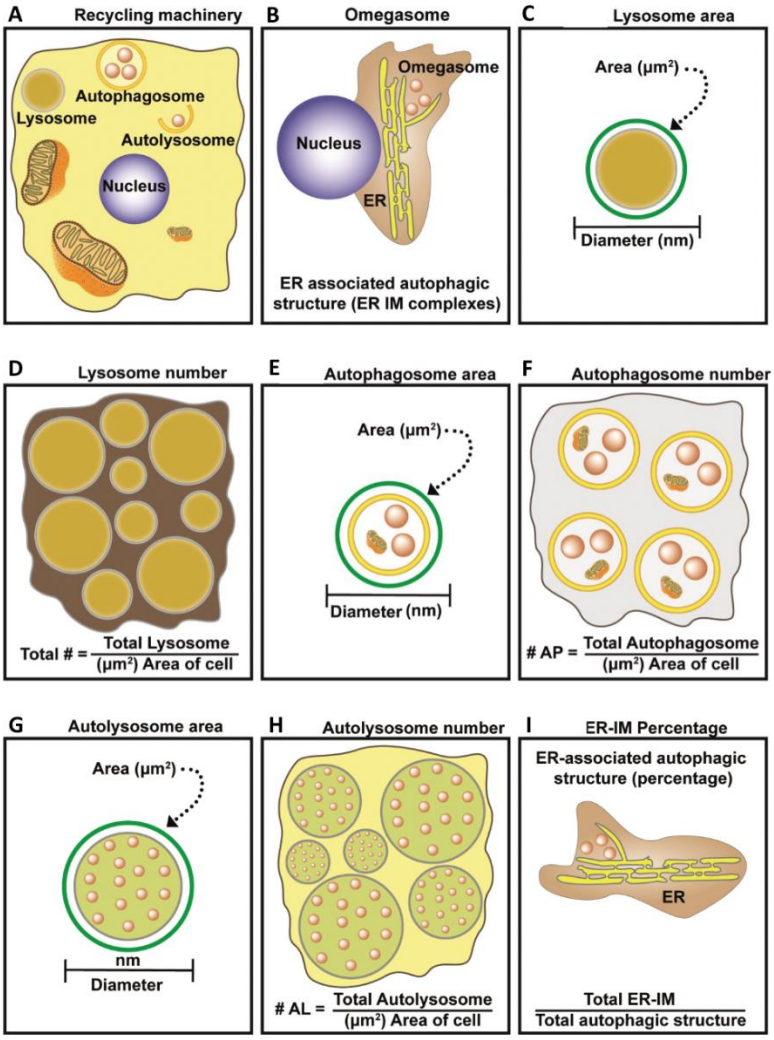

Supplemental Figure 1. Proper measurement and magnification for analyzing essential recycling machinery. To accurately assess lysosomes or autophagosomes, the lysosome and autophagosome numbers, area, and diameters should be measured. This strategy is the same strategy applied to mitochondria. (**A–I**) Magnifications should be standardized to acquire a clear understanding of the morphological changes observed in mitochondria and other organelles. Recycling machinery varies considerably in size depending on the organelle. Thus, no single magnification can encompass all structures of interest. For example, omegasomes can be large and require each structure to be individually quantified relative to the endoplasmic reticulum (ER). (**A and B**) The structure and quantity of these organelles vary between cell types and across treatment conditions. (**C–H**) Alternatively, the recycling machinery, such as lysosomes, autophagosomes, and autolysosomes, can be analyzed at 1000× to measure the area, diameter (length and width), and quantity. (**I**) 1000× magnification can be used to count ER-isolation membranes (ER-IMs). To view detailed morphology, the use of magnifications lower than 4000× is recommended.

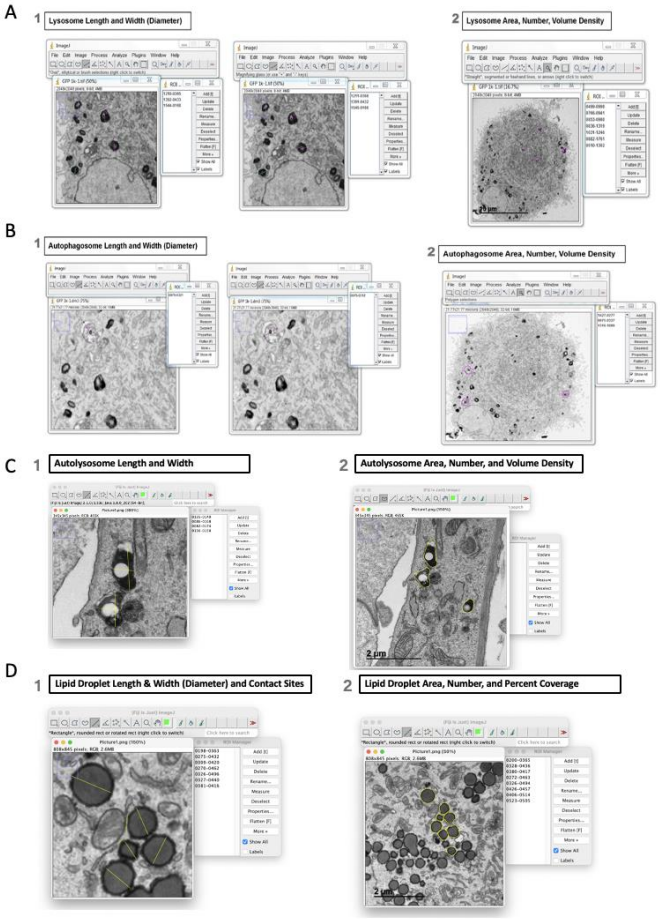

Supplemental Figure 2. Workflow and representative images of the quantification of autophagosomes, lysosomes, autolysosomes, and lipid droplets. (**A**) The fundamental process used to evaluate lysosomes using key measurements, including length, width, area, number, and density. Lysosomes are all indicated in representative images by circles quantifying area and lines spanning the Feret's diameters. (**B**) Additional representative images show the same information for autophagosomes and (**C**) autolysosomes. (**D**) Slightly differing quantifications should be performed for lipid droplets, although they may all be easily performed using ImageJ. All of these quantifications should be performed separately, on an organelle type-by-organelle type basis, to avoid the accidental confusion of regions of interest.

It is important to properly identify and distinguish degradation machinery depicted in Figures 1-5. Although under TEM without any other methods being used in tandem, degradation machinery may look similar, several key differences can be used to distinguish these structures.

- Lysosomes and autolysosomes can be misidentified because both share similar circular or elongated, ovular shapes. Additionally, when imaged via transmission electron microscopy (TEM), the membrane will appear as a black circle surrounding both lysosomes and autolysosomes. Lysosomes feature multiple membranes, which can result in an appearance similar to that of a multilamellar vesicle; however, typically, lysosomes feature fewer membranes and contain more evident enzymes than multilamellar vesicles. Traditional lysosomes feature defined membranes containing permeases and a lighter interior filled with enzymes. Although lysosomes appear slightly darker, they still have a mostly consistent color, whereas autolysosomes feature a clear center area, which is an indicator of having undergone fusion.
- Autophagosomes may be mistaken for both lipid droplets and inclusion bodies, although some key differences may be observed. At a higher magnification, multivesicular bodies may also appear to feature multiple membranes; however, many multivesicular bodies contain lipids, which gives the interior compartment of multivesicular bodies an inhomogeneous appearance compared with autophagosomes. Similar to autophagosomes, multivesicular bodies can have a similar cargo-laden appearance, especially from at lower magnification. In such cases, a higher magnification can be used to identify differences between multivesicular bodies and autophagosomes.
- Autophagosomes may also be mistaken for lysosomes or other organelles. Autophagosomes without cargo can resemble lysosomes, especially if they clump. The varying stages and cargoes of autophagosomes give them varied appearances, including some with incomplete membranes, whereas others have more complete membranes and contain cargo. At high magnification, autophagosomes appear to have two or more membranes, and the cargo typically appears as defined sacs that are more circular rather than as cristae or other artifacts.
- Autolysosomes or autophagosomes can also be easily mistaken for lipid droplets due to the similar color and appearance of these two structures. Lipid droplets are typically located in a single area near the edge of the cell, which is not typical behavior for autophagosomes, which are found closer to the center of cells and rarely clump. Additionally, unlike autophagosomes, lipids have a small membrane that is barely visible in many cases. Furthermore, lipid droplets may be differentiated by a greater degree of clumping, a single, thinner membrane, and a greater diversity in sizes. Lipid droplets may appear similar to autolysosomes. Autolysosomes in an earlier stage of fusion are marked by two clear sacs.
- Multilamellar vesicles can present akin to autolysosomes. Multilamellar vesicles have many lipid bilayers, which give them a ring-like appearance. However, these rings, when examined under high magnification, have a disorganized and crooked pattern that allows for their identification. In contrast, many ovular autolysosomes feature clear, circular, white autophagosomal compartments, which are indicative of cargo contained within the autolysosomes.

Supplemental Table 1. Identification of Degradation Machinery

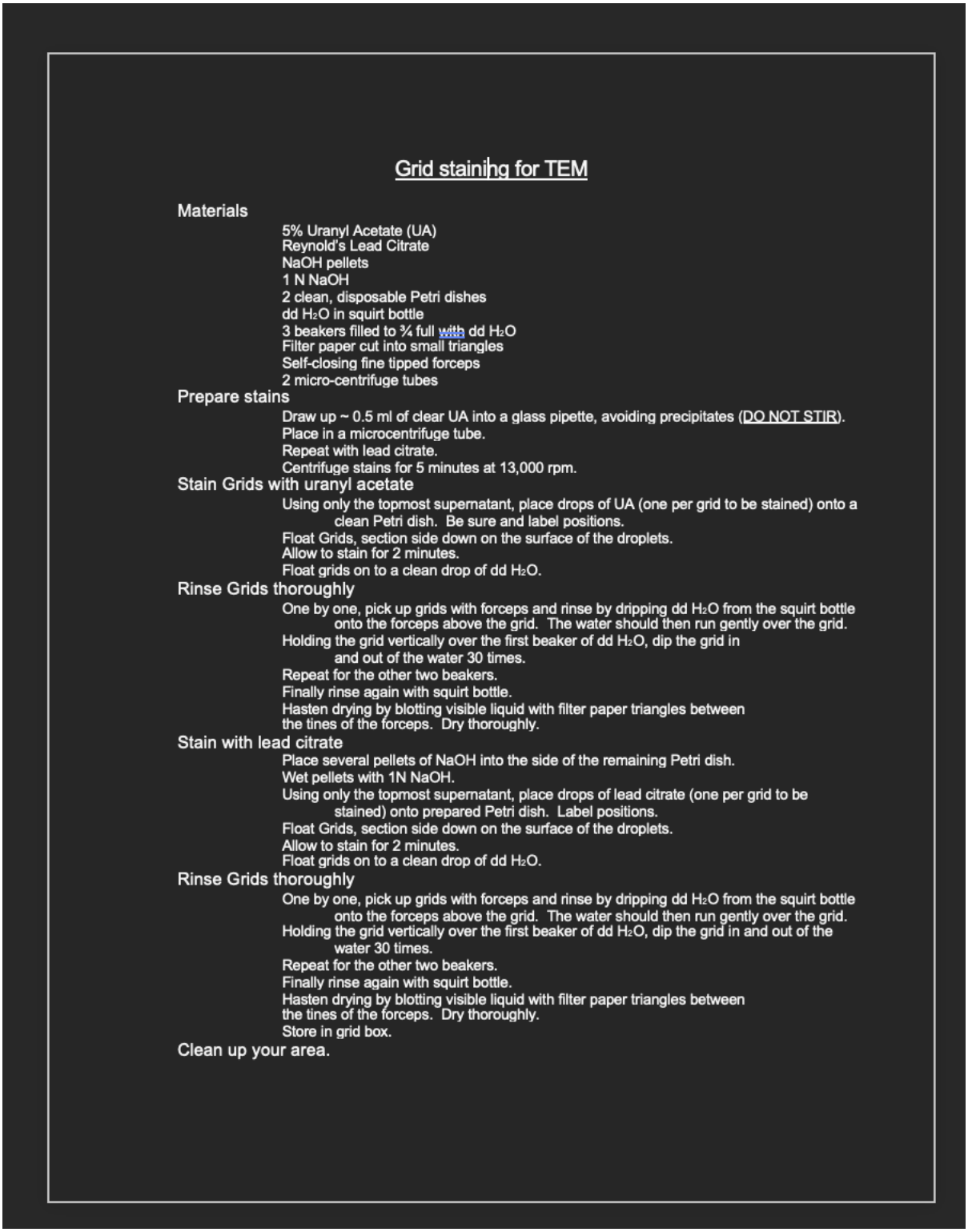

Grid staining for TEM

Materials

5% Uranyl Acetate (UA)
Reynold's Lead Citrate
NaOH pellets
1 N NaOH
2 clean, disposable Petri dishes
dd H_2O in squirt bottle
3 beakers filled to ¾ full with dd H_2O
Filter paper cut into small triangles
Self-closing fine tipped forceps
2 micro-centrifuge tubes

Prepare stains

Draw up ~ 0.5 ml of clear UA into a glass pipette, avoiding precipitates (DO NOT STIR).
Place in a microcentrifuge tube.
Repeat with lead citrate.
Centrifuge stains for 5 minutes at 13,000 rpm.

Stain Grids with uranyl acetate

Using only the topmost supernatant, place drops of UA (one per grid to be stained) onto a clean Petri dish. Be sure and label positions.
Float Grids, section side down on the surface of the droplets.
Allow to stain for 2 minutes.
Float grids on to a clean drop of dd H_2O.

Rinse Grids thoroughly

One by one, pick up grids with forceps and rinse by dripping dd H_2O from the squirt bottle onto the forceps above the grid. The water should then run gently over the grid.
Holding the grid vertically over the first beaker of dd H_2O, dip the grid in and out of the water 30 times.
Repeat for the other two beakers.
Finally rinse again with squirt bottle.
Hasten drying by blotting visible liquid with filter paper triangles between the tines of the forceps. Dry thoroughly.

Stain with lead citrate

Place several pellets of NaOH into the side of the remaining Petri dish.
Wet pellets with 1N NaOH.
Using only the topmost supernatant, place drops of lead citrate (one per grid to be stained) onto prepared Petri dish. Label positions.
Float Grids, section side down on the surface of the droplets.
Allow to stain for 2 minutes.
Float grids on to a clean drop of dd H_2O.

Rinse Grids thoroughly

One by one, pick up grids with forceps and rinse by dripping dd H_2O from the squirt bottle onto the forceps above the grid. The water should then run gently over the grid.
Holding the grid vertically over the first beaker of dd H_2O, dip the grid in and out of the water 30 times.
Repeat for the other two beakers.
Finally rinse again with squirt bottle.
Hasten drying by blotting visible liquid with filter paper triangles between the tines of the forceps. Dry thoroughly.
Store in grid box.

Clean up your area.

Supplemental Table 2. Grid Staining for TEM. Protocol for using uranyl acetate and lead citrate for grid staining.